Glassy and ballistic dynamics in collision cascades in amorphous TiO_2: Combined molecular dynamics and Monte Carlo based studies across energy scales

Alexander Holm [*] and Stefan G. Mayr [†]

Leibniz Institute of Surface Engineering (IOM), Permoserstr. 15, 04318 Leipzig, Germany
and Division of Surface Physics, Department of Physics and Earth Sciences, University of Leipzig, Linnestr. 5, 04103 Leipzig, Germany

(Received 4 December 2020; accepted 14 April 2021; published 6 May 2021)

Kinetics in amorphous TiO_2 driven by ion irradiation are discussed in the framework computer simulations. Thermal spike like regions along the path of incident ions are identified and their effects on the glassy system are described. Benefiting from the complementary approaches of purely ballistic TRIM (transport in matter) simulations and molecular dynamics simulations, a distinction between characteristic scales for short-range diffusive relocations ($\lesssim$4.5 Å) and long-range ballistic relocations is achieved. It is found that diffusion dynamics within thermally activated cascade zones sets in at the critical temperature T_c, identified as the critical temperature of the mode coupling theory, while the mean relocation limit for thermal diffusion in the glassy system is attributed to an overlap between the energy regime of purely ballistic and thermally activated relocation processes.

DOI: 10.1103/PhysRevB.103.174201

I. INTRODUCTION

In view of many promising applications, e.g., degradation of environmental pollutants, photocatalyst for CO_2 conversion, light induced water splitting, and even tissue cultivation, the transition metal oxide TiO_2 receives a considerable amount of interest [1–4]. Especially amorphous nanostructures, such as nanoparticles or nanotube arrays, open up the way for advanced technologies [5,6]. Tailoring electronic features is relevant for many of those applications, e.g., to increase the efficiency of photoactivity or increasing conductivity [3,7,8]. Ion irradiation is a reliable method to achieve this, e.g., by introducing dopants. With this method, however, there is a number of specific effects to be discussed in the context of the induced kinetics, which can influence thermal and structural stability of the amorphous system. Numerous studies on irradiating metallic glasses were performed in recent decades, based on both experimentally and modeling techniques [9–11]. The fundamental advantage of atomistic simulations is the ability to describe characteristic length and time scales to be associated with the underlying response mechanisms due to irradiation with energetic ions. Those are (i) local thermal activation, (ii) generation and annihilation of point defects as a consequence of energetic collisions, and (iii) the combination of both effects [12]. Thermal activation, also referred to as thermal spikes, occur as a collective process inside of volumes of interacting atoms affected by the collision cascade [13,14]. The scales of expansion and lifetimes of such spikes is of particular importance for structural relaxation processes of often metastable glassy systems [15]. The origin of those thermal regions is the kinetic energy dissipation of ballistically propagating energetic particles. Such collisions also have the potential to generate point defects, whose relocation dynamics scale differently from those of thermal diffusion, thus raising questions on combined effects due to the intrinsic entanglement of both mechanisms [10,12]. In turn, the diffusivity can also be effected by defects. The generalization of close Frenkel pairs in crystalline to amorphous systems are close dilution-compression centers [10,16–19]. Benefiting from such structures, high mobility characteristics can be induced. On top of that, the breaking of lattice symmetry, when comparing crystalline and amorphous structures, poses further difficulties when trying to predict long-range defect migration in highly random and long-range disordered glass structures.

In this paper we employ molecular dynamics and Monte Carlo based atomistic computer simulations to describe these highly localized processes on atomic scales. Complementary to models about thermal spikes and displacement energies in crystalline titanium oxides and steady state properties of glasses under irradiation, it is intended to reproduce effects comparable to scales of ion irradiation in experiments [20–22]. Addressing amorphous TiO_2, in the present work first we provide a scheme to obtain displacement energies for the amorphous structure, from which the corresponding values for the different atomic species are determined. Properties of the amorphous system, obtained from molecular dynamics (MD) simulations, were used as input to compute recoil energy spectra using the established TRIM (transport in matter simulations) software [23]. Owing to the nanodimensionality of the application-relevant materials described above, small penetration depths are of interest for implantation processes and thus implantation energies in the low keV regime. The determined spectra cover relevant energies over a range of three orders of magnitude. At each scale, one representative energy is picked to describe effects along the path of an irradiation induced collision cascade. With the onset of the purely

[*] alexander.holm@iom-leipzig.de
[†] stefan.mayr@iom-leipzig.de

thermal regime at the end of a collision cascade, volumes are identified which occupy atoms of elevated kinetic energy due to collision processes. The temperature in these volumes is evaluated by comparing the observed velocity distributions to according Maxwell-Boltzmann distributions and tracked vs time. Consequences of the thermal activation on the glassy system were studied by evaluating relocation statistics and referring their evoking mechanism to the competing underlying physical processes. In doing so, the results from MD and the stochastic results from TRIM simulations are used as complementary tools. Eventually, the results are discussed, focusing on glassy dynamics within the thermal spikes, referencing the critical temperature for such collective processes in the glassy system, and pointing out characteristic time and length scales for both the thermal and the ballistic regime. Throughout this work, the term relocation refers to atomic displacements due to the effects of energetic collision cascades.

II. METHODS

Classical molecular dynamics (MD) simulations, based on the LAMMPS code, were employed to study the cascade dynamics in amorphous TiO_2 [24]. The atomic interaction was implemented by fitting two potentials of different classes together, each describing a characteristic regime, depending on the interatomic separation. The equilibrium part of the atomic interaction was modeled with the Matsui-Akaogi (MA) potential, which reliably describes the structure of the three crystal polymorphs of TiO_2: rutile, anatase, and brookite [25]. The parameters for the potential are chosen to be the same as those proposed in the original work. For taking into account the high-energy part of the potential, the approach of Robinson *et al.* was implemented, viz. using the appropriate Ziegler-Biersack-Littmark (ZBL) potentials to describe interactions at small atomic separations [21,23]. The interpolation to the equilibrium part of the potential was achieved with an exponential function of the form

$$S_I = \exp\left(\sum_{i=0}^{5} a_i\, x^i\right) \tag{1}$$

to ensure continuity of the potentials as well as their first and second order derivatives at the borders of the interpolation interval [26]. The interpolation intervals are taken from Robinson *et al.* [21]: $I_{\text{Ti-Ti}} = [0.4, 1.0]$ Å, $I_{\text{Ti-O}} = [0.4, 2.4]$ Å, and $I_{\text{O-O}} = [0.6, 1.6]$ Å. To account for Coulomb interaction, the damped shifted force model described by Fennell is used [27]. To handle the Coulomb part separately by optimized LAMMPS routines, the ZBL potential was corrected by subtracting the Coulomb contribution before splining to avoid double counting of the Coulomb contributions.

Subprocesses of the irradiation induced collision cascades were modeled using the primary knock-on atom (PKA) method [28]. In doing so, the energy of either a Ti or O atom of the bulk in the simulation cell with periodic boundary conditions was set to the desired value in the low keV regime. To exclude the bias of thermo- and barostat algorithms, when studying cascade dynamics the simulated system was treated as a microcanonical ensemble (NVE) referring to conservation of the atom number, the volume, and the total energy, including the additional kinetic energy contribution of the PKA. Due to the high particle number, fluctuations occurring in this ensemble are distributed according to Maxwell-Boltzmann, as will be shown later. In the kinetic energy regime of keV, the steep slope in the repulsive part of the potential demands a small time step in order to ensure the conservation of energy. Therefore, an adaptive time step was used, such that the maximum distance to an updated position was $\leqslant 0.5$ pm. Consequently, the time step increases with the amount of transferred kinetic energy from the PKA to the embedding system. With a simulation cell containing $\approx 2 \times 10^6$ atoms, a mean kinetic energy of 5 meV is dissipated among the atoms in the simulation cell for PKA energies of 10 keV, causing no severe heating ($\approx$30 K) of the simulation cell in NVE ensemble and restricts self-interaction due to the finite size of the simulation cell. When simulating systems at predefined temperature and vanishing pressure (whenever there is no PKA cascade involved), both these quantities were controlled by Nose-Hoover thermo- and barostats, implemented according to the equations of motion of Shinoda *et al.* and the time integration schemes according to Tuckerman *et al.* [29–32]. For both the Nose-Hoover thermo- and barostate the coupling time constants were 30 fs and chain lengths of three were used.

The purely ballistic, Monte Carlo based simulations were performed with the TRIM software [23]. The density of the 500 Å expanding layer was adopted from the amorphous MD simulation cell, as well as the displacement energies obtained for Ti and O (see results). The angle of incidence for the projectile particles (Ti and O) was 0° and their initial energies were pointed out where needed. Remaining parameters were kept at default values of the program. The calculation type of "monolayer collisions" was chosen in order to generate the complete "collision" text file. From the recoil atoms trajectory, the relocation distributions for the purely ballistic displacement cascades were determined.

III. RESULTS AND DISCUSSION

A. Simulation cell and glass temperature

The simulation cells with an amorphous structure were generated by melting a rutile structure at a temperature sufficiently high above the expected melting temperature (5000 K) for a few picoseconds. The melt was then thermalized at 3000 K over a period of 30 ps and subsequently quenched at rates of 10 K/ps and 100 K/ps down to 300 K at zero pressure. The glass transition and consequently the caloric glass temperature T_g depend on the specific cooling rate of the quench [10,33]. For the quench rate of 100 K/ps the related glass temperature is $\approx$1435 K and $\approx$1530 K for the rate of 10 K/ps (the corresponding graphs can be found in the Supplemental Material [34]). The amorphous structure resulting from the lower quench rate is used as the initial configuration for subsequent simulations.

The amorphous structure of the simulation cell was additionally analyzed with the averaged Steinhardt bond-order parameter, according to Lechner and Dellago, to ensure the absence of crystalline clusters or nanocrystallites [35]. The

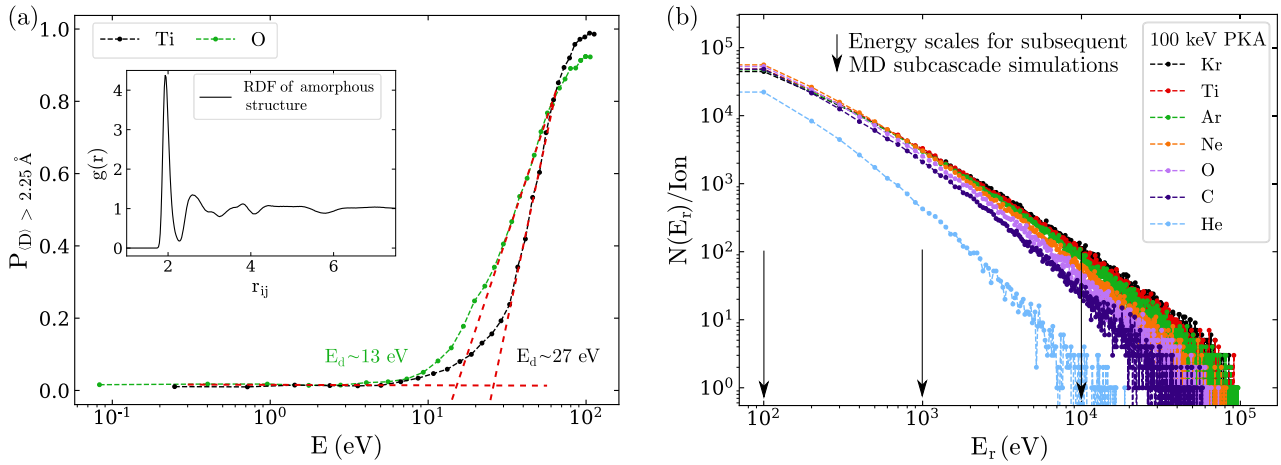

FIG. 1. (a) Probability of finding an atom displaced by at least 2.25 Å vs the provided kinetic energy. From extrapolating the tangents, the displacement energies, E_d are estimated. The inset shows the radial distribution function of the amorphous simulation cell. (b) Spectrum of the recoil energies, E_r, due to ion irradiation. The energy scales for subsequent subcascade simulations employing Ti and O as primary knock-on atoms are highlighted.

corresponding graphics for this analysis are shown in the Supplemental Material [34].

As demonstrated previously, diffusion is intrinsically not related to T_g but the critical temperature of the mode coupling theory T_c instead [36]. The suitability of this approach has been demonstrated previously by numerous experimental studies (see Ref. [[10]] for an overview). As will be shown in Sec. III D, 1492(32) K is determined to be the critical temperature of the mode coupling theory for the amorphous TiO_2 system.

B. Displacement energy

In describing cascade induced thermal spikes, volumes of high energy density are considered in which the maximum energy of a constituting atom is below a characteristic threshold value for ballistic displacements. In this regime, the energy can no further be transferred via ballistic transport processes, but thermally. The threshold value for the energy used in this work is displacement energy E_d. In crystals, a common definition for displacement or relocation thresholds is the creation of a stable Frenkel pair [21]. In the presently studied amorphous system, however, a threshold was defined as an atomic displacement of at least 2.25 Å, which is roughly the first minimum in the radial distribution function (RDF) after the amorphous nearest neighbor peak, shown in the inset of Fig. 1(a). This scenario is closely related to the crystalline vacancy-interstitial characteristic, see also Ref. [37]. Systematically, the displacement energy was determined by calculating the difference between an arbitrarily picked atoms mean position $r_{c,0}$ in the thermalized simulation cell before and after it was provided with the desired kinetic energy $r_{c,1}$. In order to determine a threshold value, several kinetic energy values need to be tested, chosen within a range around the expected threshold value. The kinetic energy to be tested was specified by scaling the velocity of the atom considered accordingly. The mean positions were computed by averaging over the atoms trajectory, covering 1 ps in the microcanonical ensemble for the thermalized cell and 0.3 ps to 0.7 ps after the velocity was set (depending on the energy: shorter time steps adept to higher energies). Eventually, the displacement ($|r_{c,1} - r_{c,2}|$) vs the kinetic energy for that atom is evaluated, shown in Fig. 1(a). This procedure was independently repeated for every Ti (2880) and O (1440) atom in the amorphous test simulation cell. Other than in crystal, there is no preferential direction in an amorphous system; it is therefore considered to be sufficient to only committing to a single direction of orientation for the energetically driven displacement. Values for the displacement energy were estimated to be $E_{d,\mathrm{Ti}} \simeq 26$ eV and $E_{d,\mathrm{O}} \simeq 13$ eV by evaluating the intersection points of the tangents. Comparing these displacement energies in the amorphous system to those obtained from studying crystalline TiO_2, one finds that the values for oxygen are similar [21]. However, the determined displacement energy for Ti is about three times smaller than in rutile, which the authors attribute to the nature of the amorphous structure, viz. the absence of long-range order, directional dependencies due to crystal symmetry and different coordination. As shown in Ref. [34], 18.8% of the Ti atom experience an undercoordination of O, whereas only 10.7% of the O atoms are undercoordinated.

C. Temperature development in thermal spike like regions

During the transition from the higher energetic ballistic regime, thermal events occur at the end of collision cascades [38]. When focusing on these, to be shown important effects it is reasonable to find a suitable decomposition of the whole irradiation induced cascade to avoid unnecessary use of computational resources and improve statistics. Concluding from the recoil energy spectrum generated by 100 keV purely ballistic TRIM cascades, a relevant subset of energies was identified: 100 eV, 1 keV, and 10 keV, shown in Fig. 1(b). Those are used as incident energies for the modeling of high energy collision cascade subprocesses. The 100 keV input energy and cross section of different ionic species for the TRIM cascades were chosen as arbitrary representatives for low keV implantation experiments.

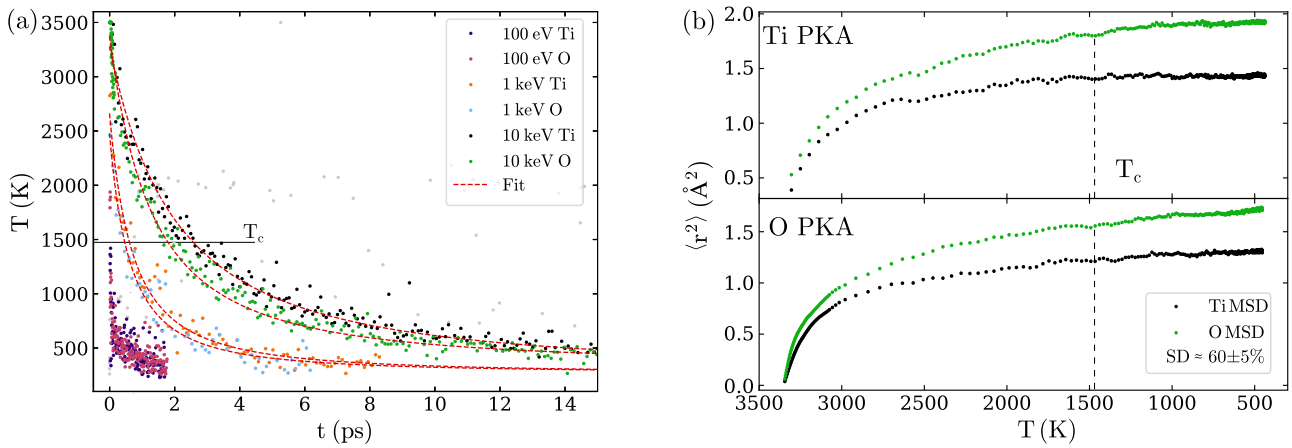

FIG. 2. (a) Temperature development in visually predetermined thermal spike like regions of highest energy density due to dissipated energy of the collision cascade in the microcanonical ensemble, discriminating the responses to Ti and O primary knock-on atoms. The fit corresponds to the time development of the heat kernel. $T_c \simeq 1492(32)$ K denotes the critical temperature of the mode coupling theory. The temperature is represented by the Maxwell-Boltzmann velocity distribution of the thermally activated atoms. (b) Development of the atomic mean squared displacement in the predefined thermal spike volumes due to 10 keV Ti and O PKAs. The time-temperature relationship is established by the fit, shown in (a).

From visual inspection of the collision cascades at a certain time step, one can identify centers of energy which is due to the PKA having already covered a certain distance in the simulation cell and lost energy to atomic collisions. The volumes of interest are around these centers, where the temperatures above T_c occur as a consequence of high energy density [9]. Such volumes caused by 100 eV PKA energies expand over a diameter of approximately 25 Å in every spatial direction, whereas volumes caused by 1 keV and 10 keV PKA energies expand over ≈30 Å. Notably, the 10 keV cascades produce multiple volumes of high energy density, whereas only single volumes of elevated energy density are observed for the lower energies studied. Therefore, at incident energies above 10 keV but still in the low keV regime, self-similarities are expected [39,40]. An exemplary snapshot of a simulation cell displaying the path of a 10 keV PKA is shown in the Supplemental Material [34]. Due to generally irregular shapes, the volumes of high energy density were approximated with spherical regions of 15 Å radius around a center of energy identified by visual inspection, covering ≈1300 atoms. To address temperature, the velocity based kinetic definition is used, which establishes the connection between kinetic energy E_k and temperature

$$E_k = \tfrac{3}{2} k_B T, \tag{2}$$

where k_B is the Boltzmann constant and T the temperature. However, single particle dynamics differ from the thermodynamics of ensembles. Therefore, similar to the scheme of Zhu, Averback, and Nastasi [38], to characterize temperatures and their development in such a cascade core volume, its properties were compared to the appropriate Maxwell-Boltzmann (MB) statistics for the velocity distributions:

$$f_T(v) = 4\pi \left(\frac{m_{\mathrm{Ti/O}}}{2\pi\ k_B T}\right)^{\frac{3}{2}} |\mathbf{v}_{\mathrm{Ti/O}}|^2\ \exp\left(-\frac{m_{\mathrm{Ti/O}}\ |\mathbf{v}_{\mathrm{Ti/O}}|^2}{2\ k_B T}\right) \tag{3}$$

at different time steps, where $m_{\mathrm{Ti/O}}$ is the mass of the respective Ti or O subsystem and $\mathbf{v}_{\mathrm{Ti/O}}$ the corresponding velocity. Thermal spikes of a particular temperature are identified as regions that reveal a Maxwell-Boltzmann distribution of that particular temperature. The starting point for the computation of the velocity distribution time series was determined by the event of the maximum kinetic energy of an atom associated with the thermal spike dropping below the lowest displacement energy, which is $E_{d,\mathrm{O}}$. An example for such a velocity distribution can be found in the Supplemental Material [34].

Initially, the observed distributions appear as a combination of two superposed MB distributions at different temperatures, corresponding to two regions. The hot region is characterized by temperatures exceeding several hundred Kelvin. This is a manifestation of high kinetic energies due to preceding recoil events of the collision cascade and consequently the thermal spike. The cold region is interpreted as a part of the unaffected environment being inside the spherical core volume due to the irregular shape of the actual cascade. After ≈1 ps, the shoulder, indicating a separation between hot and cold region, disappears as the velocity distributions approach the shape of a single MB distribution due to thermalization.

The thermal spike shows a temperature decrease in periods of several picoseconds. An analysis via fitting of the decaying temperature reveals that the temperature development can be described by the fundamental solution to the heat equation, also referred to as a heat kernel

$$K(t, x, y) = \frac{1}{(4\pi t)^{d/2}}\ \exp\left(\frac{-|x-y|^2}{4Ct}\right), \tag{4}$$

with d being the dimension, t the time, x and y representing spatial coordinates, and C a constant of dimension $m^2 s^{-1}$ to ensure correct dimensionality [41]. The fitting function depicted in Fig. 2(a) was obtained by setting the appropriate dimension and focusing on the center of the thermal excitation, $|x-y| = 0$. Within the transition period from the ballistic to the thermal regime in the cascade volumes investigated, temperatures of up to 3500 K are observed for the 10 keV collision cascades, 2500 K for the 1 keV cascades,

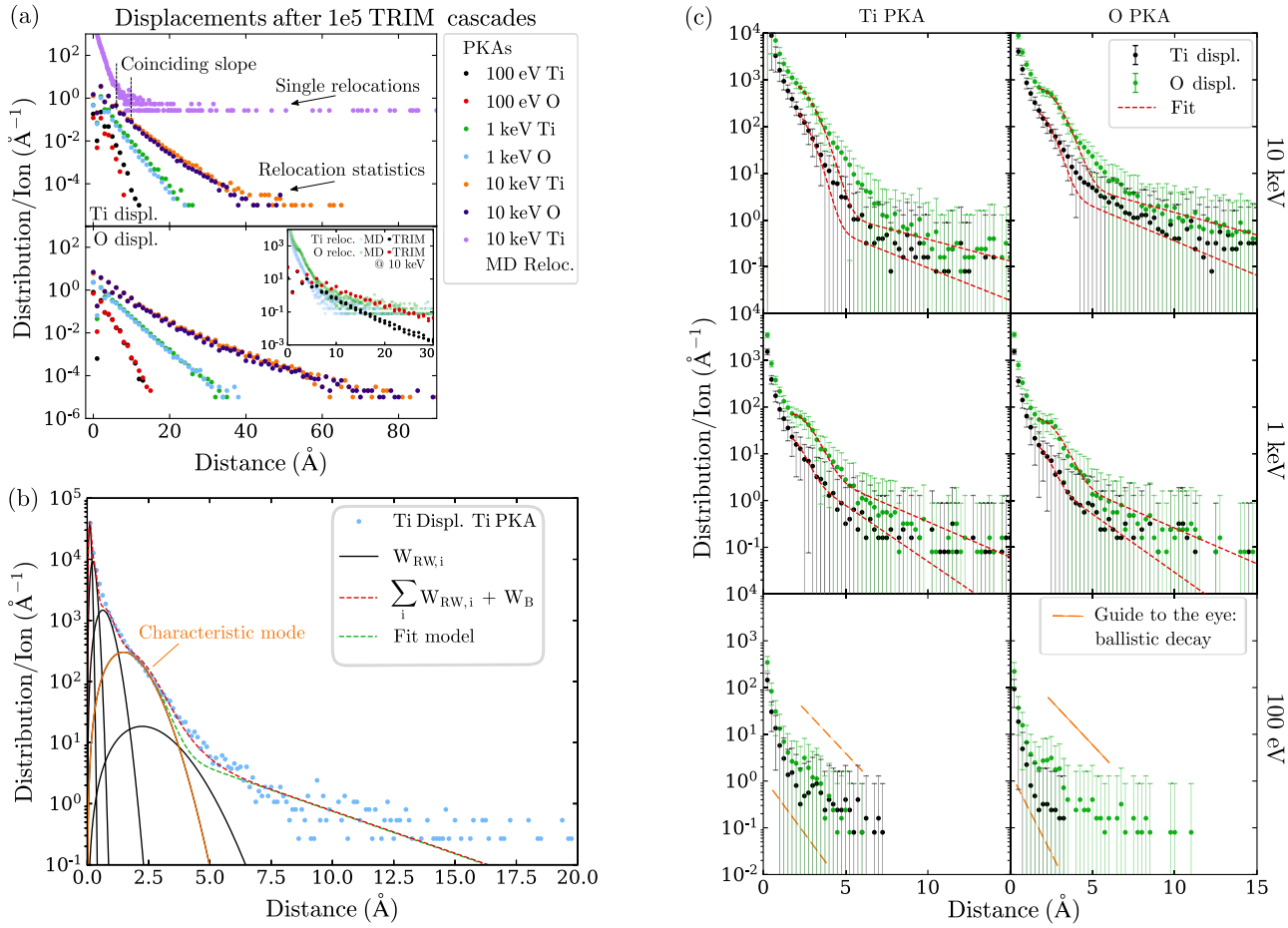

FIG. 3. (a) Relocation distributions obtained from purely ballistic TRIM trajectories and an exemplary MD distribution for direct comparison. Long-range relocations in MD are only single events, resembling poor statistics. (b) Schematic representation for the decomposition of the entire relocation distribution into several subdistributions for thermally activated random walk propagation and ballistic propagation. (c) Mean relocation distributions after 100 completed O and Ti MD collision cascades induced by primary knock-on atoms at different energies. As the fit, Eq. (11), indicates, the distribution in the range fitted resembles a superposition of ballistic and thermally activated diffusion. The error bars represent the standard deviation of the average.

and 2000 K for the 100 eV cascades. For the 1 keV and 10 keV cascades, these values unambiguously exceed the critical temperature of the mode coupling theory. However, in the further course of the development rapid cooling is observed in all cases studied. After approximately 1.8 ps to 2.6 ps the thermal spike temperature fell below the critical temperature in the 10 keV collision cascades and after 0.5 ps to 0.6 ps in the case of 1 keV cascades, shown in Fig. 2(a). Within the margin of accuracy, for the 100 eV cascade one can only state that thermal activation near the critical temperature occurs for a few hundred femtoseconds.

The duration of the thermal spike being above T_c differs marginally depending on the primary knock-on atoms species: When using O PKAs, the cooling is slightly faster compared to Ti PKAs. General differences in terms of PKA species can, on one hand, be accounted for by the highly stochastic character of individual cascades and melt volumes around collision centers. On the other hand, however, the qualitative differences, e.g., in cooling rates between Ti and O PKA induced cascades, shown in Fig. 2(a), and total number of atoms relocated, shown in Fig. 3(a), can also be explained by the difference in scattering cross sections of Ti and O atoms. As a simple approximation the model of colliding hard spheres of diameter $d_{1,2}$ is applied

$$\sigma_{1,2} = \frac{\pi}{4}(d_1 + d_2)^2 \text{ with } 1,2 = \text{Ti,O}. \tag{5}$$

When using the nuclear radii of Ti and O one obtains: $\sigma_{\text{O-O}} = 4.52$ Å^2, $\sigma_{\text{Ti-O}} = 13.46$ Å^2, and $\sigma_{\text{Ti-Ti}} = 27.15$ Å^2. This means that over the same mean path, the probability of Ti atoms to scatter with other atoms is higher than for O. When comparing cascade volumes, the energy density therefore is higher in thermally activated volumes due to Ti PKAs as a result of the increased number of collisions. Consequently, the temperature gradient between the surface of the high energy thermal spike volume and the environmental atoms takes longer to reach the inner part of the volume, which, hence, decreases the cooling rate of the thermal spike.

The close range structure remains undisturbed by the thermal spike, as concluded from comparing partial RDFs of the thermal spike region before and after the collision cascade took place [34]. Additionally, a topological analysis based on the above described averaged version of the Steinhardt bond-order parameter shows that there is no formation of

crystalline clusters as a consequence of the considered thermal spikes [34].

D. Distinguishing relocation mechanisms

The temperature analysis indicates that the contribution of purely thermal diffusion to relocation dynamics must be restricted to times of a few picoseconds and volumes composed of several hundred atoms. To further evaluate the irradiation induced effects and point out the impact of thermal diffusion, the atomic relocations compared to the initial configuration were determined after 100 eV, 1 keV, and 10 keV collision cascades at 0 K. To improve statistics, the average over multiple cascades was considered for each energy and PKA species. For TRIM simulations, 10^5 collision cascades were realized and 100 for MD. The resulting distributions are shown in Fig. 3.

When comparing the obtained distributions from MD to crystalline systems, one recognizes the absence of the oscillatory behavior for relocations within a few lattice constants [12]. This is attributed to the glass state of the system: With the absence of lattice periodicity there are no preferential relocation sites. The majority of the simulated atoms are in a displacement range close to 0 Å, shown in Figs. 3(b) and 3(c), indicating that they were not relocated in the sense of producing a defect that significantly affects coordination properties. Small relocations can be attributed to athermal processes, such as accommodation of local stresses arising from ballistically induced defects.

As shown in the distributions in Fig. 3(c) due to collision cascades induced by 1 keV and 10 keV PKAs, larger relocation distances can be further decomposed into an athermal ballistic part and a diffusive part due to thermal activation. The incorporated relocation mechanisms for diffusive and ballistic propagation are of physically fundamentally different nature, thus evoking different characteristic length scales [12]. Ballistic diffusion refers to particles with kinetic energies which are above the displacement energy, such that they are able to propagate along their trajectory in between scattering events. An extensive description can be found in Ref. [42]. This is compared to the mechanism of thermally activated diffusion. As a consequence of cooperative motion, particles show the characteristics of random walk behavior. In collision cascades of sufficiently high energy, both mechanisms are encountered [12].

For ballistic relocations the associated distribution follows an exponential decay behavior [9,12,43,44].

$$W_B(r_{\mathrm{Ti/O}}) = B\ \exp\left(-\frac{|r_{\mathrm{Ti/O}}|}{L_b}\right), \tag{6}$$

where $r_{\mathrm{Ti/O}}$ are relocation distances observed for the Ti or O subsystem, the coefficient B acts as a parameter, describing the number of constituents to the distribution, and L_b has the physical interpretation of a mean relocation distance. Purely ballistic cascade dynamics were first examined with TRIM simulations, as the stochastic approach lacks the influence of temperature and ensemble dynamics. The resulting distributions after 10^5 simulated cascades are shown in Fig. 3(a), agreeing with the assumption of the exponentially decaying distribution [Eq. (6)].

Also displayed, in the inset of this figure, there is the direct comparison between normalized MD and TRIM relocation distributions due to 10 keV PKAs, achieved by overlaying. One obtains an interval ranging from approximately 5 Å to 15 Å, in which the exponential decay coincides. Beyond this interval, there are only single relocations contributing to the MD histogram due to insufficient sampling of long-range displacement events during the total of 100 MD collision cascades simulated. The higher number of realized TRIM cascades improves the statistic for long-range relocations significantly.

At lower distances the thermal effects dominate the relocation distribution in the MD data. Thermally activated diffusion shows the characteristics of random walk propagation, which can be described by a $r^2_{\mathrm{Ti/O}}$ weighted Gaussian-type distribution, also referred to as the angular integral of the Van Hove self correlation function [45,46]

$$W_{\mathrm{RW}}(r_{\mathrm{Ti/O}}) = A\ r^2_{\mathrm{Ti/O}}\ \exp\left(-\frac{r^2_{\mathrm{Ti/O}}}{R^2_{\mathrm{RW}}}\right). \tag{7}$$

The coefficient A, again, acts as a parameter, describing the number of constituents to the distribution, and R^2_{RW} is a characteristic relocation distance of dimension m^2. Physical interpretation of the R^2_{RW} parameter is substantiated by calculating the expectation value for the mean squared displacement $\langle r^2 \rangle$ (MSD) as well as the position of the maximum r_m according to the statistic in Eq. (7). The solution yields

$$\left\langle r^2_{\mathrm{Ti/O}} \right\rangle = \frac{\int_0^\infty r^2_{\mathrm{Ti/O}} \cdot W_{\mathrm{RW}}(r_{\mathrm{Ti/O}})\,\mathrm{d}r}{\int_0^\infty W_{\mathrm{RW}}(r_{\mathrm{Ti/O}})\,\mathrm{d}r} = \frac{3}{2} R^2_{\mathrm{RW}} \tag{8}$$

$$r_{m,\mathrm{Ti/O}} = \sqrt{R^2_{\mathrm{RW}}} \tag{9}$$

and shows that both quantities are predetermined by R^2_{RW}.

To discriminate between the thermal and athermal processes and gain enhanced understanding of the physics underlying the relocation mechanisms evoked by the kinetics in the collision cascades, a comprehensive analysis of the MD distributions, shown in Fig. 3(c), is performed. Preliminary, the diffusive part has to be understood as a superposition of random walk distributions differing in their coefficients A and characteristic mean relocations governed by R^2_{RW}. This is due to the spectrum of thermal activation along the path of the collision cascade. Thermal-spike-like regions intrinsically differ in size and temperature. On this premise, a complex distribution composed of multiple random walk distributions has to be considered

$$W_{\mathrm{RW},i}(r_{\mathrm{Ti/O}}) = \sum_i A_i\ r^2_{\mathrm{Ti/O}}\ \exp\left(-\frac{r^2_{\mathrm{Ti/O}}}{R^2_i}\right). \tag{10}$$

An example for such a combined distribution with few arbitrarily chosen R^2_{RW} modes and coefficients is shown in Fig. 3(b). The term mode is adapted in this context to discriminate between random walk distributions with different values for R^2_{RW}. As a conclusion from the proposed scheme of superposed distributions one can identify a characteristic mode, further on R^2_{C}. This mode is distinguishable by the coefficient and high R^2_{RW} value, when applied to the observed relocation distributions. The combination of this characteristic

TABLE I. Characteristic coefficients and mean relocation distances as parameters of the fit according to the relocation distributions in Eq. (6) for the purely ballistic part and Eq. (11) for the combination of the ballistic thermal diffusion part. It is distinguished between primary knock-on atom type and displacements within the atomic subsystem ($\delta_{\mathrm{Ti/O}}$). The intervals for fitting are described in the text. The errors result from the least squares fit routine.

	B/Å^{-1}	L_b/Å	A/Å^{-1}	R^2_{RW}/Å^2
1 keV Ti PKA				
δ_{Ti}	12.5(13)	1.81(2)	28(1)	1.89(3)
δ_{O}	11.5(9)	2.87(3)	58(1)	2.98(3)
1 keV O PKA				
δ_{Ti}	9.1(11)	1.74(2)	20(1)	1.78(4)
δ_{O}	8.6(6)	2.85(5)	46(2)	3.00(6)
10 keV Ti PKA				
δ_{Ti}	18.8(12)	3.12(26)	328(10)	2.24(2)
δ_{O}	26.5(17)	4.67(66)	803(15)	2.81(2)
10 keV O PKA				
δ_{Ti}	10.6(9)	2.95(26)	286(11)	2.01(3)
δ_{O}	13.2(8)	4.53(66)	588(10)	2.98(3)

mode, representing the long-range limit for thermal diffusion, and the ballistic part is used to derive a model for fitting to the averaged MD relocation distributions

$$W_{\mathrm{reloc}}(r_{\mathrm{Ti/O}}) = W_{\mathrm{RW},R_c^2}(r_{\mathrm{Ti/O}}) + W_{\mathrm{B}}(r_{\mathrm{Ti/O}}) \qquad (11)$$

to compare thermal and athermal influences. The fit procedure for the curves displayed in the graphs of Fig. 3(c) can be summed up with: (i) obtain the exponential decay L_b from TRIM data, (ii) fit the ballistic tail from 8 Å to 15 Å to obtain the ballistic coefficient B suitable for the data of relocations from MD, and (iii) fit the combined distribution in the interval from 1.8 Å to 15 Å to get R_c^2 and A, identifying the parameters for the characteristic mode of thermal relocation dynamics. The parameter values can be found in Table I.

Within the boundaries of the fit model, the contribution of thermally activated diffusion to the relocation distributions can be estimated by relating the coefficients, A and B, of the underlying distributions. One obtains that the percentage of diffusive random walk behavior is in the range of roughly 95% for PKA energies of 10 keV and 80% for PKA energies of 1 keV. The mean squared displacements corresponding to the highest thermal relocation mode is similar for both energies discussed, which is ≈2.3 Å to 3.2 Å for the Ti subsystem and ≈4.5 Å for O. Above 6 Å the relocations solely result from ballistic processes, as the distribution exceeds the steep decay of the random walk propagation and the decay matches the ballistic relocation decay. For PKAs with 100 eV, the identification of a dominant high temperature contribution is not possible, and therefore no subdivision into thermally activated and diffusive part. From the corresponding distribution in Fig. 3(c), however, it is assumed that only ballistic effects contribute significantly to the observed relocations, as the guide to the eye also indicates by comparing to the decay to ballistic distributions from TRIM.

As for PKA energies above 1 keV diffusion account for a large fraction to the relocation dynamics, the diffusivity itself as the cause for relocations is analyzed in more detail. For this purpose an auxiliary system in bulk amorphous TiO_2 structure was prepared, consisting of 17 280 atoms, resembling an isobaric and isothermal ensemble. For the constituting Ti and O atoms of this ensemble, the atomic displacements between their initial positions and their positions after certain time intervals were statistically evaluated and related to the characteristic random walk statistic [Eq. (7)]. This was repeated at different temperatures and for different times covered by the simulation. As expected, in the regime of purely random motion, which is the case for liquid diffusion at high temperatures, the contribution of each particle's random walk leads to the corresponding distribution. Examples can be found in the Supplemental Material file [34].

The advantage of the R^2_{RW} parameter to determine the MSD over common averaging is an enhanced accuracy due to deriving the desired quantity directly from the underlying physical distribution. Additionally, this opens up the possibility to directly compare the parameters of statistic models and observed relocation distributions of both the collision cascade and the auxiliary system. For glassy systems in the diffusive regime, it was already shown by Kluge and Schober [47] that the MSD shows linear behavior vs time. According to Eq. (8), the time dependence of R^2_{RW} is also expected to be linear in time, when diffusion is the case. In the plots shown in Fig. 4(a) the time developments of R^2_{RW} parameters at different temperatures are displayed. From the time development of R^2_{RW} in the linear regime for sufficiently long times (between 1 ns and 10 ns in the present study), and hence the MSDs, the diffusivity is determined by the well known relation to the MSD ($\langle r^2(t)\rangle_{\mathrm{Ti/O}}$)

$$D_{\mathrm{Ti/O}} = \lim_{t\to\infty} 1/6\ \partial_t \left\langle r^2_{\mathrm{Ti/O}}(t)\right\rangle_{\mathrm{Ti/O}}. \qquad (12)$$

As shown in the Arrhenius plot in Fig. 4(b), the critical temperature of the mode coupling theory is determined by fitting the diffusivity in the high temperature regime to the equation obtained by mode coupling theory [36]

$$D_{\mathrm{Ti/O}}(T) \propto |T - T_{c,\mathrm{Ti/O}}|^{\gamma_{\mathrm{Ti/O}}}. \qquad (13)$$

It predicts a T_c of 1492(32) K for both Ti and O, $\gamma_{\mathrm{Ti}} = 2.0(1)$ and $\gamma_{\mathrm{O}} = 1.7(1)$.

Based on this analysis, one can proceed with identifying the temperature regime responsible for the relocation behavior

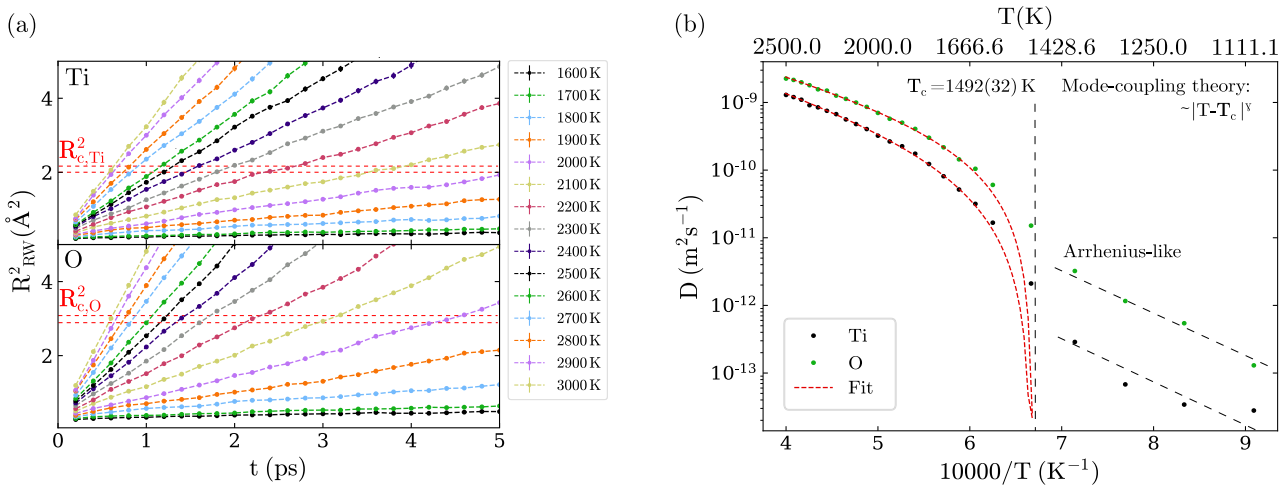

FIG. 4. (a) Time development of the mean relocation parameter R from Eq. (7) at different temperatures. The error bars correspond to the errors according to the least squares fits of the distributions. The dashed line indicates the parameter value thermal relocation limit obtained from the MD simulations. (b) Arrhenius plot of the diffusion coefficients. The critical temperature of the mode-coupling theory, obtained by fitting to Eq. (13), characterizes the transition region of low-temperature and high-temperature diffusive behavior.

observed in the cascades. This can be achieved by comparing the R_c^2 parameter to those R_{RW}^2 parameters obtained from fitting to the random walk statistics of the auxiliary glassy bulk system. In the final completely thermalized state of the simulation cell, R_c^2 carries the information of the long-range limit of thermally induced relocations. The numerical values for R_c^2, as listed in Table I, are 1.78 Å^2 to 2.24 Å^2 for the Ti atomic subsystem and 2.81 Å^2 to 3.00 Å^2 for the O atomic subsystem. These values cannot be attributed to thermal spike temperatures occurring during the completely thermal phase of the collision cascades. The short times of thermal excitation in those are insufficient to develop relocation distributions that match the high values of R_c^2.

This observation is substantiated by evaluating the time development of the atomic mean squared displacement inside a thermal spike. Beginning at the end of ballistic phases due to 10 keV PKAs, in Fig. 2(b) the MSD is plotted vs the temperature. The major contribution to particle displacements, being above 92% of the thermalized values, is accomplished before the ensemble temperature drops below T_c. Therefore, diffusivity in the thermal regime of the collision cascade shows significant dependence on T_c. The absolute MSD values obtained from this analysis, again, do not compare with those predicted by the characteristic mode R_c^2 for the thermal relocation limit. However, relocations evoked during the purely thermal phase can be attributed to different modes in the short range part of the MD relocation distribution, shown in Fig. 3(b). Those employ smaller R_{RW}^2 parameter values in the range of approximately 1.0 Å, as deduced from the MSD in Fig. 2(b) and according to Eq. (8).

Concluding from both the analysis of the R parameter and the MSD, relocation dynamics in the purely thermal part at the end of the collision cascade cannot explain the characteristic mode for random walk relocation dynamics occurring during the 1 keV and 10 keV cascades. Being in line with the framework of defect induced diffusivity in crystals and glasses, the authors point out the established mechanism which combines energies of the ballistic regime and cooperative motion: radiation enhanced diffusion [17–19,48]. The reason for pointing out this mechanism is the distinct interval in the MD relocation distributions, which shows the characteristics of thermally activated random walk statistics on one hand, yet being distinguishable from purely ballistic displacements on the other hand. This suggests cooperative motion within collision cascade volumes, despite being in the energy regime associated with ballistic propagation processes, as thermal diffusion at temperatures related to the observed thermal spike temperatures cannot explain relocations associated with the observed distributions. For such mechanisms, however, high energy densities are required, which can be exemplified by the 100 eV PKA induced cascades, since in these cases no significant thermal activation occurs.

IV. CONCLUSION

Thermal spikes and atomic relocations as response to 100 eV, 1 keV, and 10 keV ion irradiation of amorphous TiO_2 were studied. Pointing out characteristic ranges, displacements above ≃6 Å are attributed to ballistic processes only. Up to this threshold, displacements are evoked by radiation enhanced diffusion as an interplay of cooperative ballistic propagation and thermal diffusion. The later process shows dependencies on the critical temperature of the mode coupling theory, which is determined to be 1492(32) K. However, lifetimes of thermal spikes do not exceed 2.6 ps even for the highest energy densities due to 10 keV collision cascades.

ACKNOWLEDGMENTS

The computations were performed at the Center for Information Services and High Performance Computing (ZIH) at TU Dresden. A.H. and S.G.M. acknowledge funding by the European Social Fund (ESF) and the Development Bank of Saxony (SAB). A.H. acknowledges Prof. Dr. André Anders for valuable suggestions on aspects of the manuscript

and proofreading. A.H. also acknowledges Dr. Carsten Bundesmann for interpreting TRIM simulations and performing complementary SD.Trim.SP simulations, not presented in this work.

[1] M. Humayun, F. Raziq, A. Khan, and W. Luo, Modification strategies of TiO_2 for potential applications in photocatalysis: A critical review, Green Chem. Lett. Rev. **11**, 86 (2018).

[2] I. Rossetti, A. Villa, M. Compagnoni, L. Prati, G. Ramis, C. Pirola, C. L. Bianchi, W. Wang, and D. Wang, CO_2 photoconversion to fuels under high pressure: Effect of TiO_2 phase and of unconventional reaction conditions, Catal. Sci. Technol. **5**, 4481 (2015).

[3] V. Etacheri, C. Di Valentin, J. Schneider, D. Bahnemann, and S. C. Pillai, Visible-light activation of TiO_2 photocatalysts: Advances in theory and experiments, J. Photochem. Photobiol. C **25**, 1 (2015).

[4] V. Dallacasagrande, M. Zink, S. Huth, A. Jakob, M. Müller, A. Reichenbach, J. A. Käs, and S. G. Mayr, Tailoring substrates for long-term organotypic culture of adult neuronal tissue, Adv. Mater. **24**, 2399 (2012).

[5] L. Sang, Y. Zhao, and C. Burda, TiO_2 nanoparticles as functional building blocks, Chem. Rev. **114**, 9283 (2014).

[6] P. Roy, S. Berger, and P. Schmuki, TiO_2 nanotubes: Synthesis and applications, Angew. Chem. Int. **50**, 2904 (2011).

[7] H. H. Pham and L.-W. Wang, Oxygen vacancy and hole conduction in amorphous TiO_2, Phys. Chem. Chem. Phys. **17**, 541 (2015).

[8] H. H. Pham and L.-W. Wang, Electronic structures and current conductivities of B, C, N and F defects in amorphous titanium dioxide, Phys. Chem. Chem. Phys. **17**, 11908 (2015).

[9] R. S. Averback and T. Diaz De La Rubia, Displacement damage in irradiated metals and semiconductors, Phys. Solid State **51**, 281 (1997).

[10] F. Faupel, W. Frank, M.-P. Macht, H. Mehrer, V. Naundorf, K. Rätzke, H. R. Schober, S. K. Sharma, and H. Teichler, Diffusion in metallic glasses and supercooled melts, Rev. Mod. Phys. **75**, 237 (2003).

[11] K. Nordlund, S. J. Zinkle, A. E. Sand, F. Granberg, R. S. Averback, R. E. Stoller, T. Suzudo, L. Malerba, F. Banhart, W. J. Weber *et al.*, Primary radiation damage: A review of current understanding and models, J. Nucl. Mater. **512**, 450 (2018).

[12] R. A. Enrique, K. Nordlund, R. S. Averback, and P. Bellon, Simulations of dynamical stabilization of Ag–Cu nanocomposites by ion-beam processing, J. Appl. Phys. **93**, 2917 (2003).

[13] F. Seitz and J. S. Koehler, Displacement of atoms during irradiation, Solid State Phys. **2**, 305 (1956).

[14] H. Rath, B. N. Dash, A. Benyagoub, and N. C. Mishra, Sensitivity of anatase and rutile phases of TiO_2 to ion irradiation: Examination of the applicability of coulomb explosion and thermal spike models, Sci. Rep. **8**, 11774 (2018).

[15] P. Bellon and G. Martin, Driven alloys, Phys. Solid State **50**, 189 (1996).

[16] J. Frenkel, Über die Wärmebewegung in festen und flüssigen Körpern (german) [About the thermal transfer in solid and liquid bodies], Z. Phys. **35**, 652 (1926).

[17] S. G. Mayr, K. Samwer, and R. S. Averback, Surface kinetics during growth and ion irradiation of glassy metal films, Scr. Mater. **49**, 961 (2003).

[18] S. G. Mayr, Y. Ashkenazy, K. Albe, and R. S. Averback, Mechanisms Of Radiation-Induced Viscous Flow: Role Of Point Defects, Phys. Rev. Lett. **90**, 055505 (2003).

[19] S. G. Mayr and R. S. Averback, Surface Smoothing Of Rough Amorphous Films By Irradiation-Induced Viscous Flow, Phys. Rev. Lett. **87**, 196106 (2001).

[20] N. A. Marks, B. S. Thomas, K. L. Smith, and G. R. Lumpkin, Thermal spike recrystallisation: Molecular dynamics simulation of radiation damage in polymorphs of titania, Nucl. Instrum. Methods Phys. Res., B **266**, 2665 (2008).

[21] M. Robinson, N. A. Marks, K. R. Whittle, and G. R. Lumpkin, Systematic calculation of threshold displacement energies: Case study in rutile, Phys. Rev. B **85**, 104105 (2012).

[22] S. G. Mayr, Impact of ion irradiation on the thermal, structural, and mechanical properties of metallic glasses, Phys. Rev. B **71**, 144109 (2005).

[23] J. F. Ziegler and J. P. Biersack, The stopping and range of ions in matter, in *Treatise on Heavy-Ion Science* (Springer, Boston, MA, 1985), pp. 93–129.

[24] S. Plimpton, *Fast Parallel Algorithms for Short-Range Molecular Dynamics*, Tech. Rep. (Sandia National Labs., Albuquerque, NM, 1993).

[25] M. Matsui and M. Akaogi, Molecular dynamics simulation of the structural and physical properties of the four polymorphs of TiO_2, Mol. Simul. **6**, 239 (1991).

[26] R. Smith, D. Bacorisen, B. P. Uberuaga, K. E. Sickafus, J. A. Ball, and R. W. Grimes, Dynamical simulations of radiation damage in magnesium aluminate spinel, $MgAl_2$ O_4, J. Phys. Condens. **17**, 875 (2005).

[27] C. J. Fennell and J. D. Gezelter, Is the Ewald summation still necessary? pairwise alternatives to the accepted standard for long-range electrostatics, J. Chem. Phys. **124**, 234104 (2006).

[28] M. J. Norgett, M. T. Robinson, and I. M. Torrens, A proposed method of calculating displacement dose rates, Nucl. Eng. Des. **33**, 50 (1975).

[29] S. Nosé, A unified formulation of the constant temperature molecular dynamics methods, J. Chem. Phys. **81**, 511 (1984).

[30] W. G. Hoover, Canonical dynamics: Equilibrium phase-space distributions, Phys. Rev. A **31**, 1695 (1985).

[31] W. Shinoda, M. Shiga, and M. Mikami, Rapid estimation of elastic constants by molecular dynamics simulation under constant stress, Phys. Rev. B **69**, 134103 (2004).

[32] M. E. Tuckerman, J. Alejandre, R. López-Rendón, A. L. Jochim, and G. J. Martyna, A Liouville-operator derived measure-preserving integrator for molecular dynamics simulations in the isothermal–isobaric ensemble, J. Phys. A **39**, 5629 (2006).

[33] I. Prigogine, *Thermodynamics of Irreversible Processes* (Thomas, New York, 1955).

[34] See Supplemental Material at http://link.aps.org/supplemental/10.1103/PhysRevB.103.174201 for the volume (enthalpy) vs temperature plots from which the glass temperature at different quench rates was determined, for a structure characterization

with the averaged version of the Steinhardt bond-order parameter, according to Lechner and Dellago, for the ti-o and o-ti coordination histograms in the amorphous structure, for a visualization of a 10 keV PKA induced collision cascade and the connection between high energy centers and modes in the relocation distribution, for an exemplary Maxwell-Boltzmann fit of the velocity distribution in a region of high energy density, for an analysis of the effects of the thermal spike on the amorphous structure, and for exemplary time series of atomic relocations due to random walk propagation in the liquid state .

[35] W. Lechner and C. Dellago, Accurate determination of crystal structures based on averaged local bond order parameters, J. Chem. Phys. **129**, 114707 (2008).

[36] W. Gotze and L. Sjogren, Relaxation processes in supercooled liquids, Rep. Prog. Phys. **55**, 241 (1992).

[37] F. Lehnert and S. G. Mayr, Nanoporous amorphous Ge–Si alloys–unraveling the physics behind ion beam induced morphogenesis, Phys. Chem. Chem. Phys. **19**, 23461 (2017).

[38] H. Zhu, R. S. Averback, and M. Nastasi, Molecular dynamics simulations of a 10 keV cascade in β-NiAl, Philos. Mag. A **71**, 735 (1995).

[39] J. C. Moreno-Marin, U. Conrad, H. M. Urbassek, and A. Gras-Marti, Fractal structure of collision cascades, Nucl. Instrum. Methods Phys. Res., B **48**, 404 (1990).

[40] K. Nordlund, J. Peltola, J. Nord, J. Keinonen, and R. S. Averback, Defect clustering during ion irradiation of GaAs: Insight from molecular dynamics simulations, J. Appl. Phys. **90**, 1710 (2001).

[41] N. Berline, E. Getzler, and M. Vergne, *Heat Kernels and Dirac Operators* (Springer Science & Business Media, Berlin, 2003).

[42] G. Martin and P. Bellon, Radiation effects in concentrated alloys and compounds: Equilibrium and kinetics of driven systems, C. R. Phys. **9**, 323 (2008).

[43] G. Demange, E. Antoshchenkova, M. Hayoun, L. Lunéville, and D. Simeone, Simulating the ballistic effects of ion irradiation in the binary collision approximation: A first step toward the ion mixing framework, J. Nucl. Mater. **486**, 26 (2017).

[44] R. A. Enrique and P. Bellon, Compositional Patterning In Systems Driven By Competing Dynamics Of Different Length Scale, Phys. Rev. Lett. **84**, 2885 (2000).

[45] J.-N. Roux, J.-L. Barrat, and J.-P. Hansen, Dynamical diagnostics for the glass transition in soft-sphere alloys, J. Phys. Condens. Matter **1**, 7171 (1989).

[46] C. Gaukel and H. R. Schober, Diffusion mechanisms in undercooled binary metal liquids of $Zr_{67}Cu_{33}$, Solid State Commun. **107**, 1 (1998).

[47] M. Kluge and H. R. Schober, Diffusion and jump-length distribution in liquid and amorphous $Cu_{33}Zr_{67}$, Phys. Rev. B **70**, 224209 (2004).

[48] R. S. Averback and H. Hahn, Radiation-enhanced diffusion in amorphous Ni-Zr alloys, Phys. Rev. B **37**, 10383 (1988).